Peer-reviewed version available at *Materials* **2019**, *12*, 1799; doi:10.3390/ma12111799

Type of the Paper (Article)

Multi-Scale Physical-Chemical-Mechanical Characteristics of Marine Mortar, Part I—Primary Performance

Yajun WANG[1,2]*, Chuhan ZHANG[3]*, Jinting WANG[3], Yanjie XU[3], Feng JIN[3], Youbo WANG[2]*, Qian YAN[2], Tao LIU[2], Xiaoqing GAN[4], Zhan XIONG[2]

[1] Zhejiang Key Laboratory of Offshore Marine Engineering Technology, Zhoushan 316002, China; aegis68004@163.com
[2] School of Port and Transportation Engineering, Zhejiang Ocean University, Zhoushan 316002, China; wlxmwyjup@zju.edu.cn
[3] State Key Laboratory of Hydroscience and Hydraulic Engineering, Tsinghua University, Peking 100084, China; zch-dhh@tsinghua.edu.cn
[4] Yangtze River Scientific Research Institute, Wuhan, 430010, China; gxqxf@sina.com
* Correspondence: aegis68004@163.com

Abstract: Marine mortar was the goal material and its multi-scale physical-chemical-mechanical characteristics were the principal interest in this study. The on-line multi-scale damage detection experiments art was designed to quantify the characteristics mathematically and graphically. The normal cylinder specimen with 70-day age was produced and investigated by dynamically global MSHCT scan and local detection of EDS, SEM and XRD. The experiments results indicated that the marine mortar offered the appreciable strength at the early age at least, although some saline minerals were generated during the preparation. The micro-interfacial behavior and the parental foci controlled the damage development of the marine mortar the performance of which was still the adjustable one by the composition optimization.

Keywords: marine mortar; multi-scale; interfacial behavior; strength; damage; on-line detection

1. Introduction

The worldwide production of the cement-base materials is skyrocketing (Figure 1).

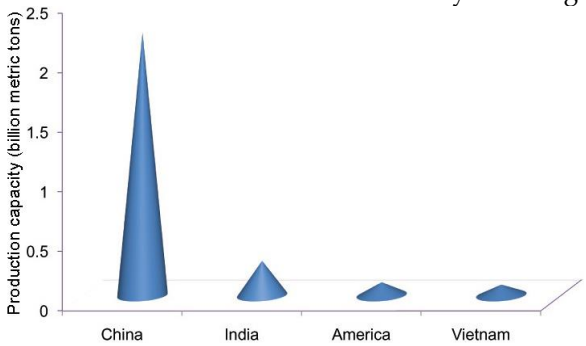

Figure 1. World cement production in 2018 [1]

The application of water and sand plays the key role in the production of the cement-base materials. The global sand consumption nowadays reaches 45 billion metric tons per year [2]. Meantime, the worldwide resource of the fluvial-lacustrine sand is being exhausted (Figure 2).

Peer-reviewed version available at Materials 2019, 12, 1799; doi:10.3390/ma12111799

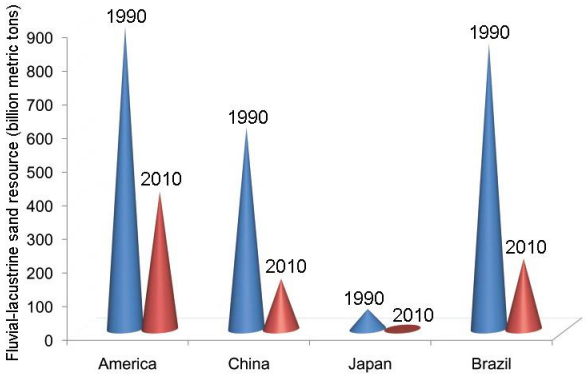

Figure 2. World fluvial-lacustrine sand resource [3]

Moreover, the fresh water also shows the growing discrepancy between the shrinking resource and the expanding consumption (Figure 3).

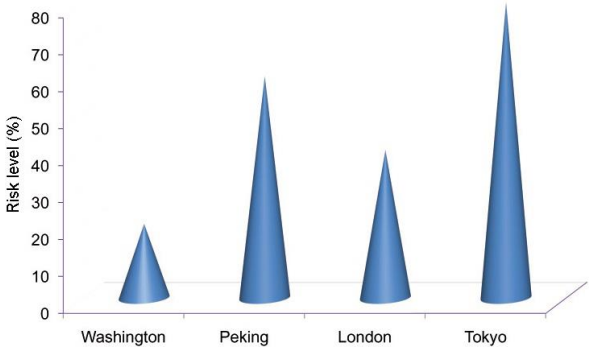

Figure 3. World water risk level after 2019 [4]

The development of the instant composites (including the instant cement-base ones) has been the crucial duty especially in the marine environment. Seawater and marine sand are the key constituents for the development of the instant cement-base composites in the offshore construction [5-8]. The seawater curing process is the preferable choice for the cement-base composites preparation in the marine environment as the result of the instant efficiency [9-11]. Wang et al. [12] carried out the multi-scale investigations on hydration mechanisms of ordinary Portland cement with seawater mixing and reported that the seawater cement paste demonstrates a highly stiffened structure for its rheological behavior at the fresh stage. Their work also mentioned that the formation of Friedel's salt encourages the future studies on chemistry between seawater and cements to beneficially utilize the seawater ingredients to improve the material properties and structural durability. Shi et al. [13] conducted the chloride ingress experiment to measure the Friedel' salt profiles in the mortar samples and their results reported that maximum amount of Friedel's salt was found in the region with limited leaching of calcium. Yu et al. [14] carried out the mechanical tests to study the effect of seawater mixing on the properties of potassium magnesium phosphate cement paste and reported that adding some mineral admixtures into the goal paste prepared with seawater could lessen the negative effect of seawater for mixing on the properties of hardened body. Similarly, Yang et al. [15] proposed the addition of limestone powder and silica fume in the magnesium potassium phosphate cement paste the early-age strength of which could be improved in seawater. Yang et al. [16] also mentioned the effect of the early seawater curing on properties of magnesium potassium phosphate cement paste and their results indicated that the performance of the goal paste cured in seawater after 3-day natural curing showed the clear improvement thanks to higher degree of crystallinity and more perfect pore size distribution. Li et al. [17] conducted the thermal experiments to investigate the properties of alkali-activated slag paste, mortar and concrete utilizing seawater and sea sand and offered the conclusion that the materials degradation is caused by thermal mismatch between paste matrix and aggregates regardless of the use of cement or slag, freshwater or seawater, and river sand or sea sand. The work of Wang et al. [18] reported that metakaolin addition improved the hydration and mechanical properties and durability of the coral waste mortar and the goal materials production can relieve the lack of locally available concrete ingredients on isolated islands. Tan et al. [19] also produced the coral aggregate seawater concrete

Peer-reviewed version available at Materials 2019, 12, 1799; doi:10.3390/ma12111799

and investigated its strength by comparison with the ones of ordinary Portland concrete and lightweight aggregate concrete. Their results proposed that the aggregate type has a significant influence on the testing strength curve of the concrete materials by different methods. Guo et al. [20] conducted the experimental investigation on the degradation of the fiber reinforced polymer which was exposed to the simulated seawater sea sand concrete environments and reported that the goal composites could stand the extreme conditions.

According to the references, it can be drawn that the marine cement-base composites have been the most popular materials in the offshore construction. Therefore, in this study, the on-line multi-scale damage detection experiments art was created and conducted to examine the multi-scale physical-chemical-mechanical characteristics of the goal marine mortar. For the experiments, the energy dispersive spectrometer (EDS) and X-ray diffraction (XRD) methods were invited to probe the chemistry of the goal marine mortar. Meantime, the thermal-field emission scanning electron microscopy (SEM) was adopted to accompany the computer tomography (CT) to trace the multi-scale performance of the goal marine mortar.

2. Materials and Methods

2.1. Composition of the Marine Mortar

We conceptualized the study ideology and designed the target marine mortar specimens' composition (Table 1) in the State Key Laboratory of Hydroscience and Hydraulic Engineering of Tsinghua University (in Peking, China). We produced the target marine mortar specimens in the Zhejiang Key Laboratory of Offshore Marine Engineering Technology of Zhejiang Ocean University (in Zhoushan, China).

Table 1. Composition of the marine mortar

Material	Amount (g)
Cement	1061
Marine sand	803
Sea water	486 (W/C=0.458)

The information on the parental materials was reported according to the composition detail as follows.

Sea water The marine mortar was prepared with the sea water that was got from Changzhi Bay of Zhoushan Seas located at 29.98º N and 122.18º E where the expectation value of pH was 7.86. The acquisition time of the seawater specimen was a.m. 9:30 on Dec 10th, 2016 and the quantitative fabric experiment lasted from a.m. 10:30 to p.m. 17:50 on Dec 10th, 2016. The quantitative fabric of the sea water specimen including the key ions and the saline minerals was shown in Figure 4.

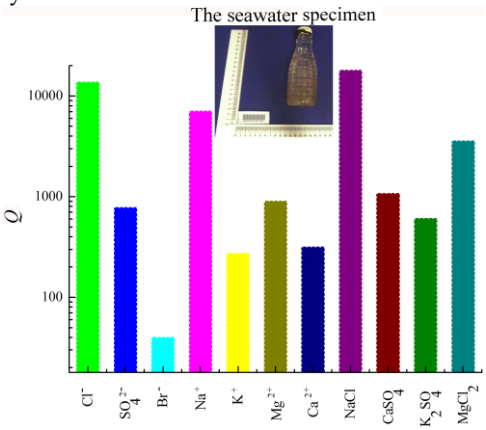

Figure 4. Quantitative distribution of the key ions and the saline minerals of the seawater specimen (The unit of *Q*, namely, the quantification, is 10^{-3}‰)

The highest concentration was the one of NaCl with 17997.65 ×10^{-3}‰ and the descending sequence of the others was Cl^- with 13768.18×10^{-3}‰, Na^+ with 7076×10^{-3}‰, $MgCl_2$ with

Peer-reviewed version available at Materials 2019, 12, 1799; doi:10.3390/ma12111799

3574.38×10^{-3}‰, $CaSO_4$ with 1074.74×10^{-3}‰, Mg^{2+} with 903×10^{-3}‰, SO_4^{2-} with 780×10^{-3}‰, K_2SO_4 with 607.66×10^{-3}‰, Ca^{2+} with 316.1×10^{-3}‰, K^+ with 272.4×10^{-3}‰ and Br^- with 40×10^{-3}‰.

Marine sand The marine sand was excavated from Nansha shore of Zhoushan seas located at 122.43º N and 29.87º E. The principal properties of the marine sand were given in Table 2.

Particularly, the natural marine sand has been treated by dryer BH-002 (power 4.5 kW, in Figure 5) for 48 hours to remove the natural water content thoroughly for the precise material design.

Figure 5. Drying process for the natural marine sand

The size distribution of the marine sand particles was investigated by both normal sieving technology (size range of 0.16 mm ~ 5 mm) and Malvern Mastersizer 2000 analyzer (size range of 0.02 ◎m ~ 2000 ◎m) and the results were offered in Figure 6. The characteristic parameters of the marine sand particles, i.e., the uniformity coefficient C_u and the curvature coefficient C_c, were defined by Equations (1) and (2) [21] and their expectation values from the statistical work were reported in Table 3. Moreover, C_u and C_c help evaluate the uniformity and the continuousness of powder materials inclusive of the marine sand particles, respectively.

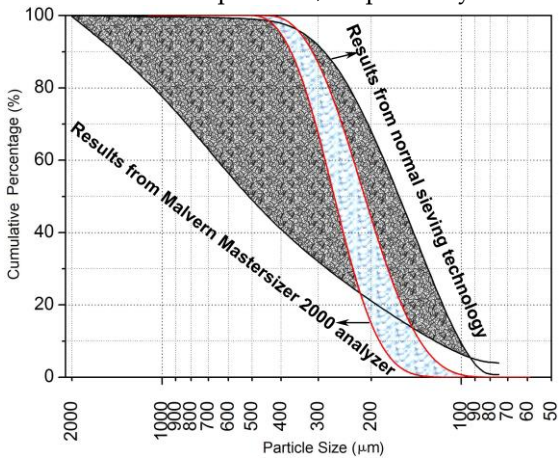

Figure 6. Size distribution of the marine sand

$$C_u = \frac{d_{60}}{d_{10}} \quad (1)$$

$$C_c = \frac{(d_{30})^2}{d_{60} \cdot d_{10}} \quad (2)$$

Peer-reviewed version available at *Materials* **2019**, *12*, 1799; doi:10.3390/ma12111799

1

Table 2. Principal properties of the marine sand

Apparent density (kg/m³)	**Packing density (kg/m³)**	**Natural water content (%)**	**Methylene blue number (‰)**	**Shell residuals contents (%)**	**Sludge contents (%)**
2652	1370.3	20%	1.4	0.23	0.27

2

3

Table 3. Expectation values of the marine sand characteristic parameters

Results from normal sieving technology						**Results from Malvern Mastersizer 2000 analyzer**					
d_{10}(μm)	d_{30}(μm)	d_{50}(μm)	d_{60}(μm)	C_u	C_c	d_{10}(μm)	d_{30}(μm)	d_{50}(μm)	d_{60}(μm)	C_u	C_c
1296	1615	2380	3054	2.36	0.66	162.617	203.008	238.943	256.571	1.58	0.99

4

Peer-reviewed version available at Materials 2019, 12, 1799; doi:10.3390/ma12111799

Particularly, d_{10}, d_{30}, d_{50} and d_{60} here designate the specific particle sizes with their cumulative composition percentages as 10%, 30%, 50% and 60% respectively.

In terms of uniformity, C_u with the value beyond 5 indicates that the material particles have the non-uniform distribution. C_u with the value below 5, by contrast, means that the material particles have the uniform distribution. With regard to continuousness, C_c with the span (1, 3) shows the continuous distribution of the material particles. Otherwise, some intermediate size groups have been lost. Hence, the marine sand of Nansha shore had the uniform and discontinuous distribution.

Meantime, the study carried out the EDS and XRD analysis to explore the marine sand composition and the results were shown in Figure 7.

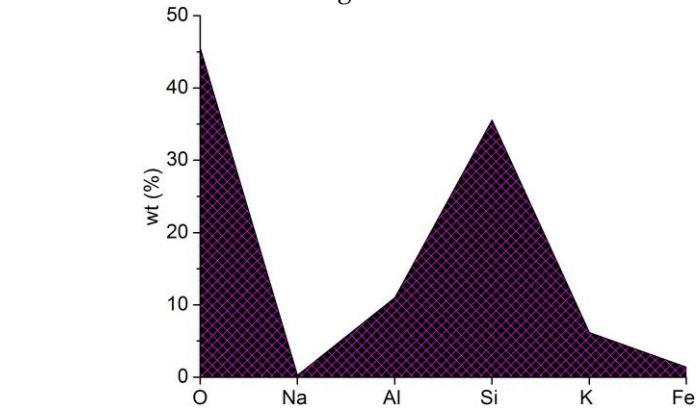

(**a**) EDS spectrum

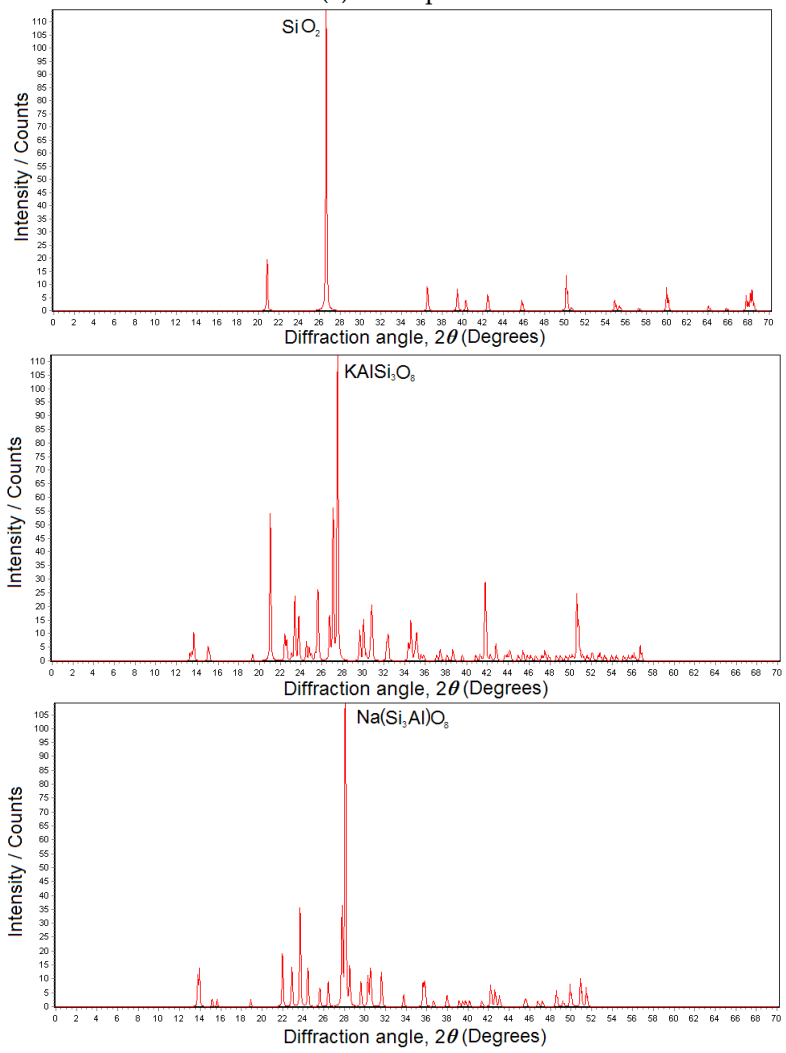

(**b**) XRD patterns

Peer-reviewed version available at Materials 2019, 12, 1799; doi:10.3390/ma12111799

Figure 7. EDS spectrum and XRD patterns of the marine sand

The SEM image of the marine sand was given in Figure 8 where SiO_2 base and the original micro-cracks were covered by $KAlSi_3O_8$ texture and $Na(Si_3Al)O_8$ chips. The irregular surface of the marine sand helped strengthen the connection between the material particle and the hydrate gel. Surely, the chip cover played X factor on the micro-interfacial behavior of the marine mortar. Hence, the micro-interfacial behavior of the marine sand and the hydrate gel should be ascertained specifically.

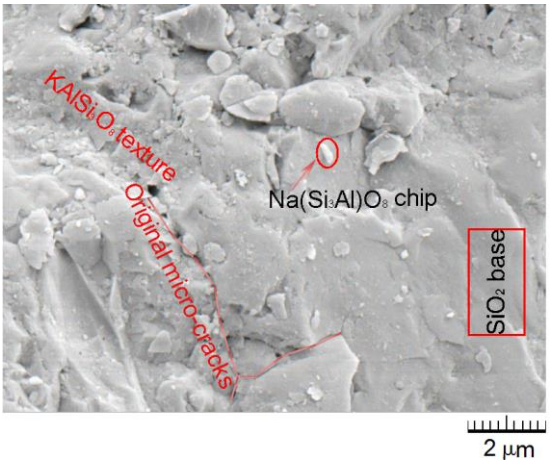

Figure 8. SEM image of the marine sand

Cement The marine mortar was prepared with the composite Portland cement P.C 42.5 R that has been produced by Hailuo Cement Co. Ltd in Southern-Eastern China and its principal properties were reported in Table 4.

Table 4. Principal properties of the composite Portland cement P.C 42.5 R

Initial setting time (minute)	Final setting time(minute)	Apparent density (kg/m^3)	Compressive strength for 28 days (MPa)
100	167	3200	55.8

EDS analysis was applied to detect the principal elements' content of the composite Portland cement P.C 42.5 R and the results were shown in Figure 9 where the values of wt% were the expectations derived from 3 scanned positions.

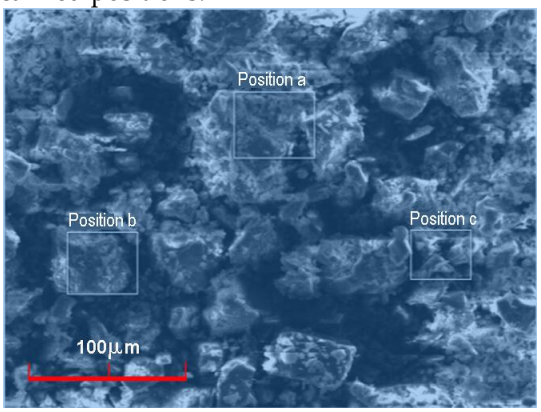

(**a**) EDS scanned positions in the composite Portland cement P.C 42.5 R micrograph

Peer-reviewed version available at *Materials* **2019**, *12*, 1799; doi:10.3390/ma12111799

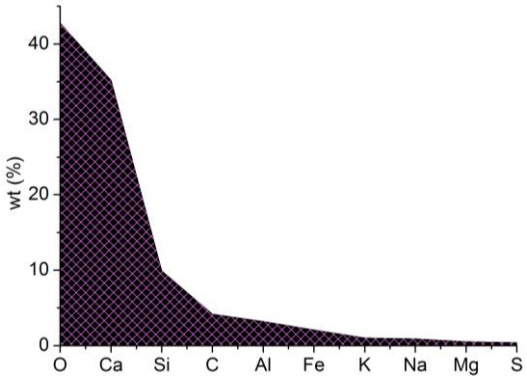

(**b**) EDS spectrum

Figure 9. Micrograph and principal elements' content from EDS analysis on the composite Portland cement P.C 42.5 R

XRD analysis was also implemented to investigate the principal composition of the composite Portland cement P.C 42.5 R and the XRD patterns were given in Figure 10.

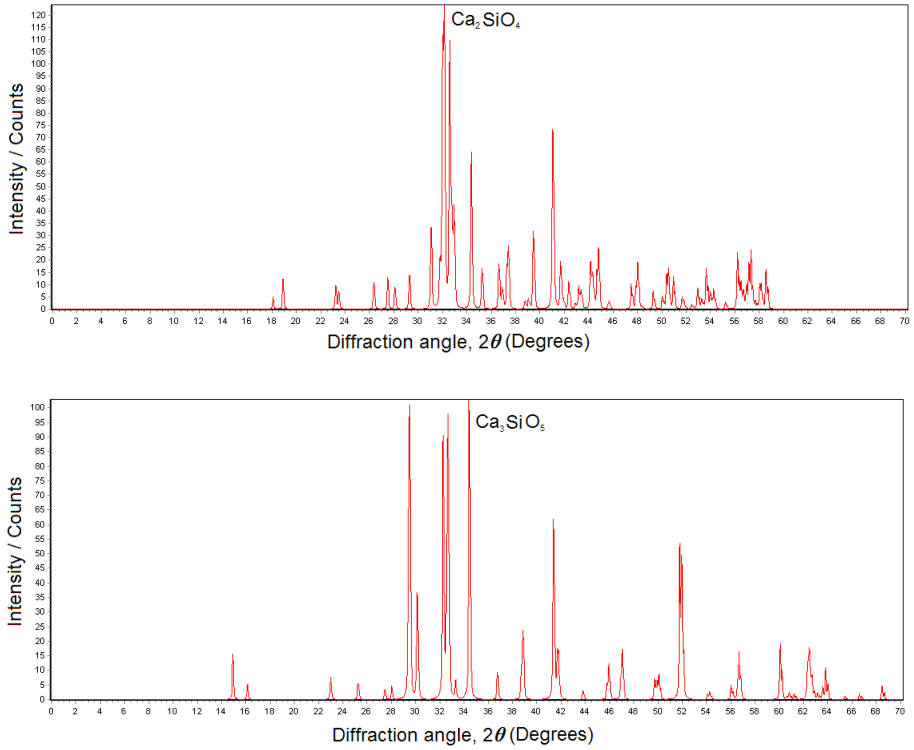

Peer-reviewed version available at Materials 2019, 12, 1799; doi:10.3390/ma12111799

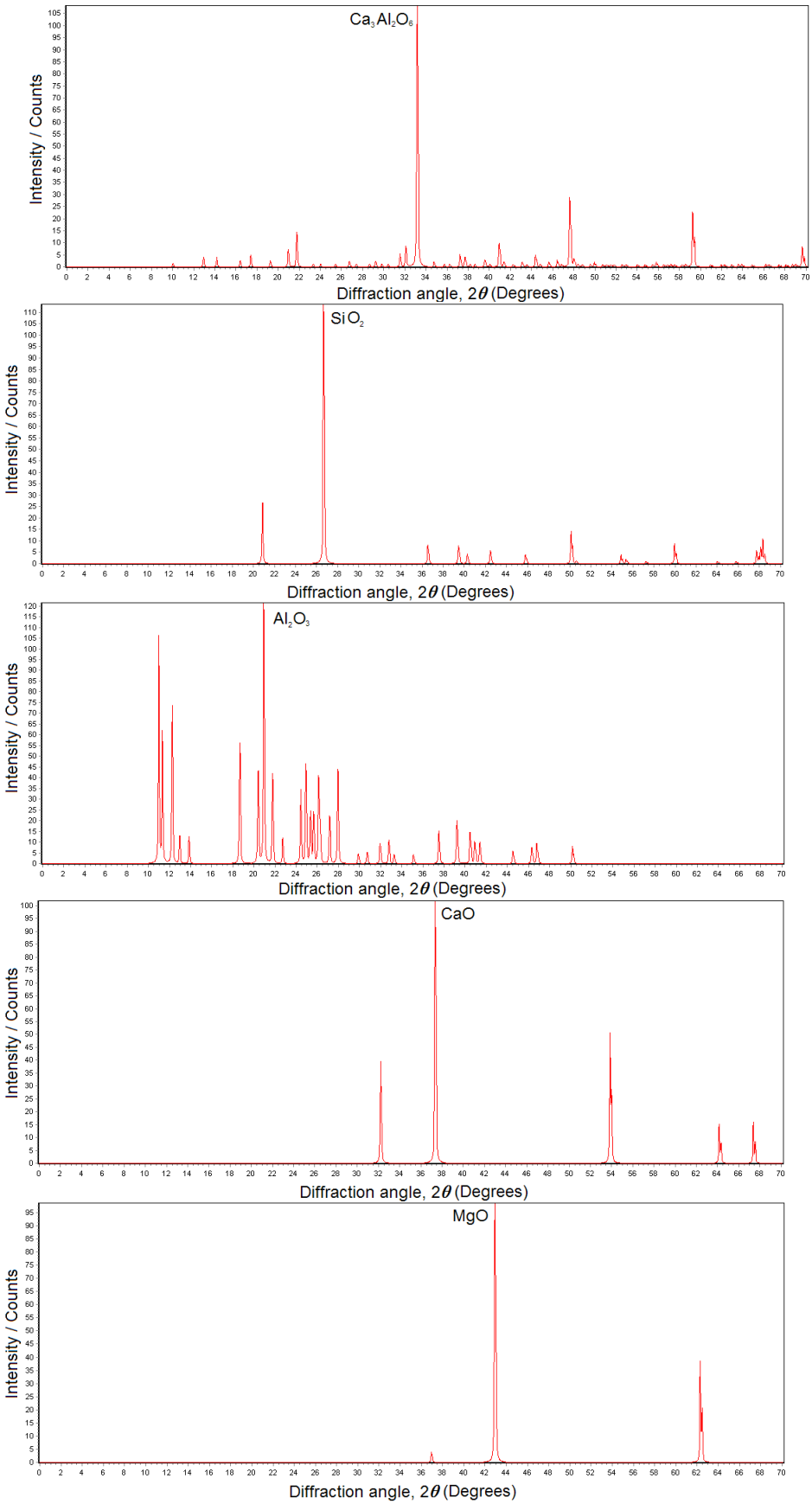

Figure 10. XRD patterns of the composite Portland cement P.C 42.5 R

2.2. Experiments' Standards, Equipments and Methods

Peer-reviewed version available at Materials 2019, 12, 1799; doi:10.3390/ma12111799

The composition design and the marine mortar specimens' preparation obey mainly the Sino standards and refer partly to the American codes [21-26].

Mixing The marine mortar paste was produced in the mixer the type of which was JJ-5 ISO679-1989(E) (maximal power 0.55 kW and capacity 5 L) produced by Jingwei company of Hebei province in China. The standard mixing time was 5 minutes.

Molding The marine mortar paste then was homogeneously poured into the normal moulds (standard dimension, i.e., length × width × height = 150mm×150 mm×150 mm) that were put on the vibroplatform for vibrating compaction (vibrating period 20 minutes, vibrating frequency 45 ± 5 Hz and vibrating amplitude 0.3 mm).

The marine mortar paste in the normal moulds rested for 24 hours indoor where the temperature and percentage relative humidity (RH) were 20 ±5 °C and 75±5%, respectively. The marine mortar specimens (namely, the cubic ones) that have achieved the initial strength then were unloaded from the normal moulds (Figure 11)

Figure 11. Marine mortar specimens unloaded from the normal moulds

Curing The unloaded marine mortar specimens were collected into the curing chamber where the temperature and percentage relative humidity (RH) were 20±5°C and 90±5%, respectively. Particularly, in order to simulate the marine environment, the cubic specimens were submerged into the tank full of the sea water that was got from Changzhi Bay of Zhoushan Seas (Figure 12). The curing age for the cubic specimens in sea water was 59 days and the total age including the resting indoor period was 60 days.

Figure 12. Sea water curing condition

Coring and cutting The marine mortar cores were then drilled from the cubic specimens by corer HZ-18B (power 2.5 kW and maximal rotational speed 1100 r / min) at 60-day age. Meanwhile, the coarse cores were cut into be the normal cylinder specimens (diameter × height = 50 mm × 100 mm) by cutter ZDQ95-8 the extreme power and the maximal dimension of the treated specimen of which were 11 kW and length × width × height =3000 mm × 1200 mm × 150 mm, respectively (Figure 13).

Peer-reviewed version available at *Materials* **2019**, *12*, 1799; doi:10.3390/ma12111799

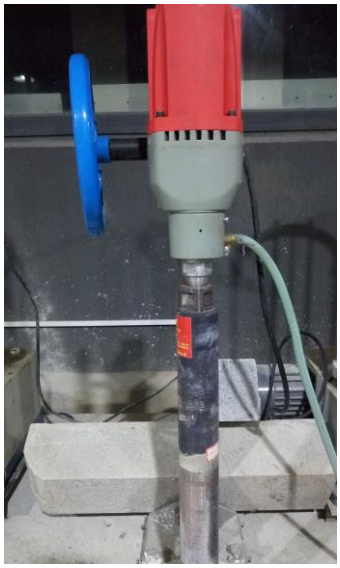

(**a**) Corer HZ-18B

(**b**) Cutter ZDQ95-8

(**c**) Cylinder specimens

Figure 13. Production of the normal cylinder specimens

Furthermore, the normal cylinder specimens of the marine mortar were re-collected into the curing chamber and re-submerged into the tank full of the sea water for another 10-day cure until they achieved 70-day age.

Tri-axial CT scanner system The on-line multi-scale damage detection experiments have been implemented by the tri-axial CT scanner system which includes two parts, namely, the strain-controlled tri-axial sub-system and the PHILIPS Brilliance 16 Multi-Slices Helical CT (MSHCT) sub-system. Table 5 showed the principal parameters of the tri-axial CT scanner system.

Peer-reviewed version available at *Materials* **2019**, *12*, 1799; doi:10.3390/ma12111799

1

Table 5. Principal parameters of tri-axial CT scanner system

(a) tri-axial sub-system

Outline dimensions (mm)	Tri-axial cabinet		Extreme loading conditions		Maximal stroke of vertical main-shaft (mm)	Accuracies (%)	
	Diameter (mm)	Height (mm)	Force from vertical main-shaft (kN)	Confining pressure (MPa)		Deformation controller	Loading controller
Height: 700 Maximal diameter: 305 Minimal diameter: 225	50	100	500	20	150	0.05	0.1

2

(b) MSCT sub-system

Gantry mouth diameter (mm)	Coverage width of detector axis Z (mm)	Gantry gradient	Detector material	Detectors sum	Detector channels sum	Detector cooling method	Scanning space accuracy (mm)	Message transmission rate (GB/s)	X-ray generator		
									Power (kW)	Maximal amperage (mA)	Maximal voltage (kV)
700	24mm	±30°±0.5°	Express rare earth ceramics	672	1344	Air cooling one	0.75	1.1	60	500	140

Peer-reviewed version available at *Materials* **2019**, *12*, 1799; doi:10.3390/ma12111799

(c) MSCT sub-system

X-ray generator			Contrast resolution (%)	Spatial resolution (mm)	Image reconstruction matrix dimension	CT value span	Contrast resolution	Spatial resolution (mm)
Power (kW)	Maximal amperage (mA)	Maximal voltage (kV)						
60	500	140	0.3	0.2	1024×1024	[-1024, 3071]	0.3%	0.2

3

Peer-reviewed version available at Materials 2019, 12, 1799; doi:10.3390/ma12111799

The axial load σ_a was executed with the rigid condition by the vertical main-shaft made by DCCr12Mov steel and the principal stress σ_1 was generated in the marine mortar in the same direction of the axial load. The confining load σ_c was conducted with the soft condition by the oil pressure that was worked on the HDPE (High Density Polyethylene) jacket (Figure. 14) the thickness and the density of which were 1mm and 0.963 g/cm^3, respectively. Meantime, the principal stress σ_2 was produced in the marine mortar in the same direction of the confining load.

Figure 14. Normal cylinder specimen covered with HDPE jacket

The term 'on-line' indicates that the normal cylinder specimens can be scanned by MSHCT during the tri-axially loading procedure to detect visually and dynamically the multi-scale damage evolution in it. Therefore, the synchronization of the multi-scale visualization and metrization can be carried out to investigate the damage evolution of the marine mortar (Figure 15).

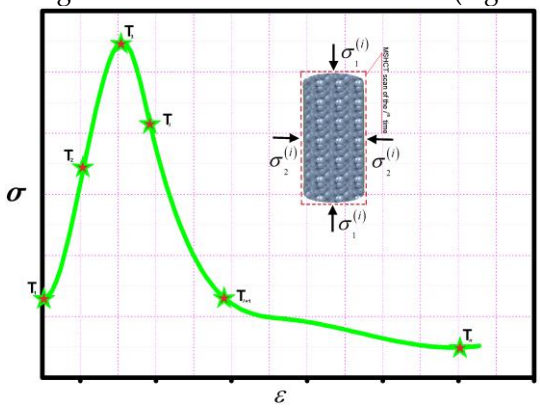

Figure 15. Synchronization of the multi-scale visualization and metrization

(T_i on the strain and stress curve was the corresponding position of MSHCT scan of the ith time and n was the total of MSHCT scan (n = 6 in the study). ε and σ represented the strain and stress states (i.e., SSS) of the marine mortar. $\sigma_1^{(i)}$ and $\sigma_2^{(i)}$ designated the principal stress states of the ith time. Particularly, the SSS that could quantified the damage mathematically and the MSHCT images that could quantified the damage graphically were collected synchronically by the help of the tri-axial CT scanner system)

Moreover, the thickness of the scanned films of the normal cylinder specimen was determined by the resolution adjustment experiments to be 3 mm uniformly (Figure 16).

Peer-reviewed version available at Materials 2019, 12, 1799; doi:10.3390/ma12111799

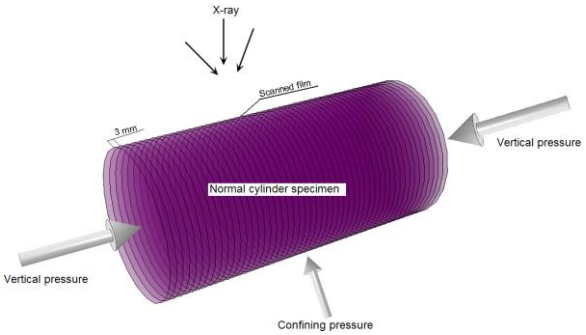

Figure 16. On-line multi-scale damage detection model

3. Results and Discussion

This section may be divided by subheadings. It should provide a concise and precise description of the experimental results, their interpretation as well as the experimental conclusions that can be drawn. The SSS was the key approach for the study of the multi-scale physical-chemical-mechanical characteristics of the marine mortar and the SSS of the marine mortar was shown in Figure 17 where ε_a, ε_v and ε_r denoted the axial strain, the volumetric strain and the radial one, respectively. Hence, the 1st, 2nd and 3rd curves expressed the relations of the principal stress σ_1 on ε_a, ε_v and ε_r, respectively. Moreover, the cyan rectangles on the three curves of Figure 14 represented the positions of MSHCT scan and the sequence of the positions of MSHCT scan was prescribed by the serial number T_i (i =1~6) and the blue arrows along the 1st, 2nd and 3rd curves. Meantime, specified on the three curves of Figure 17 were 6 marginal points, namely, A, B, C, D, E and F that, indicated by the pink circles, helped define the critical states of the multi-scale physical-chemical-mechanical characteristics of the marine mortar.

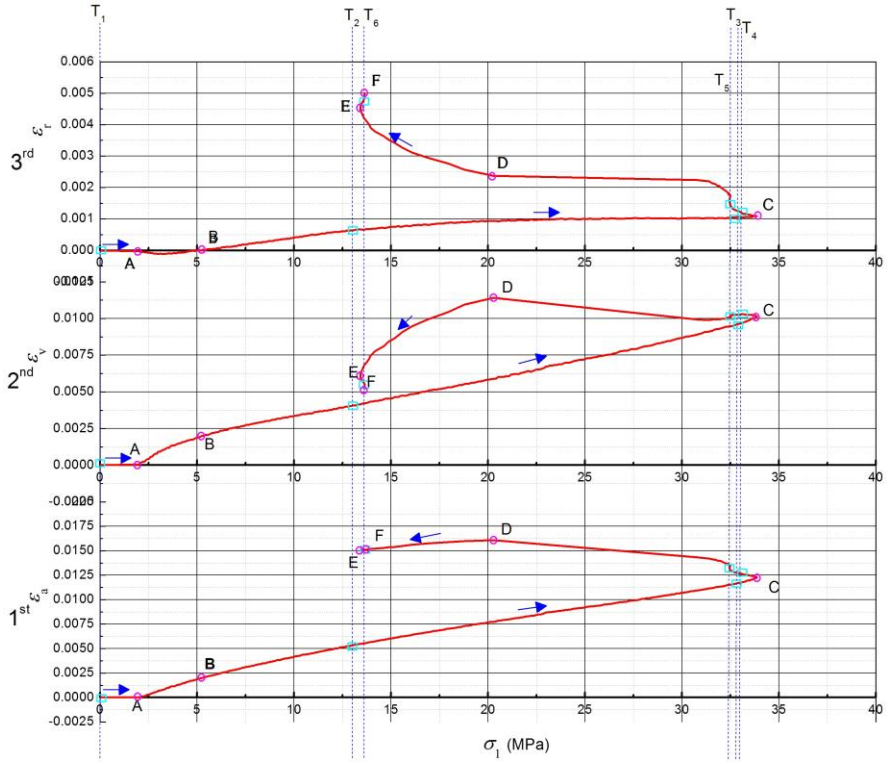

Figure 17. Multi-scale strain and stress states (SSS) of the marine mortar

The on-line multi-scale damage evolution was reconstructed by MSHCT approach and the results were given in Figure 18 where the 2-dimensional behaviors of the damaged marine mortar were presented dynamically at 6 MSHCT scan positions, namely, T_1, T_2, T_3, T_4, T_5 and T_6 where the correspondingly intrinsic fractures were detected, measured and reconstructed.

Peer-reviewed version available at *Materials* **2019**, *12*, 1799; doi:10.3390/ma12111799

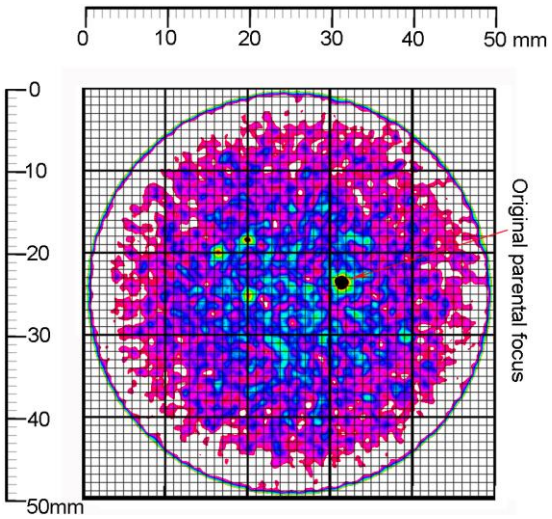

(**a**) State of T_1

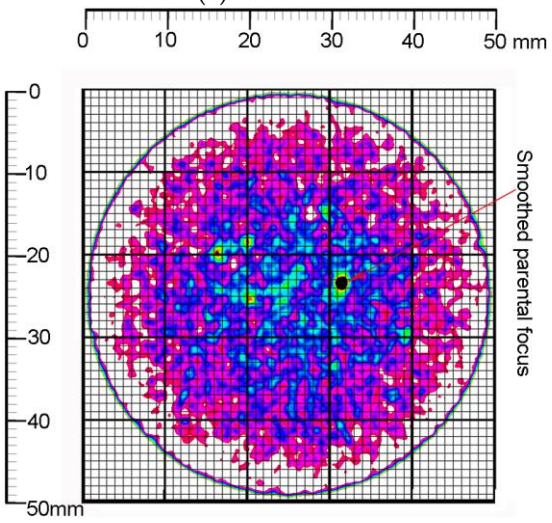

(**b**) State of T_2

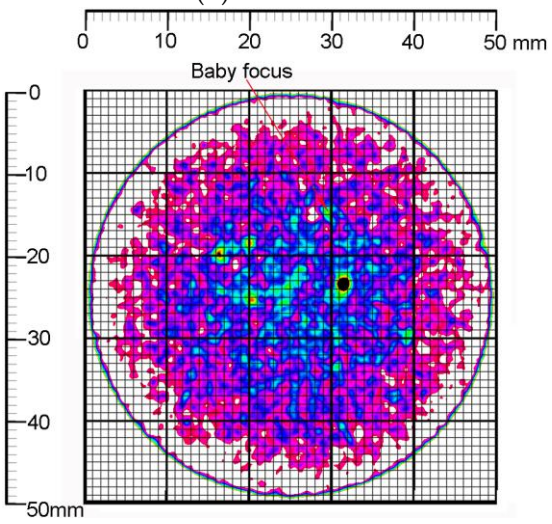

(**c**) State of T_3

Peer-reviewed version available at Materials 2019, 12, 1799; doi:10.3390/ma12111799

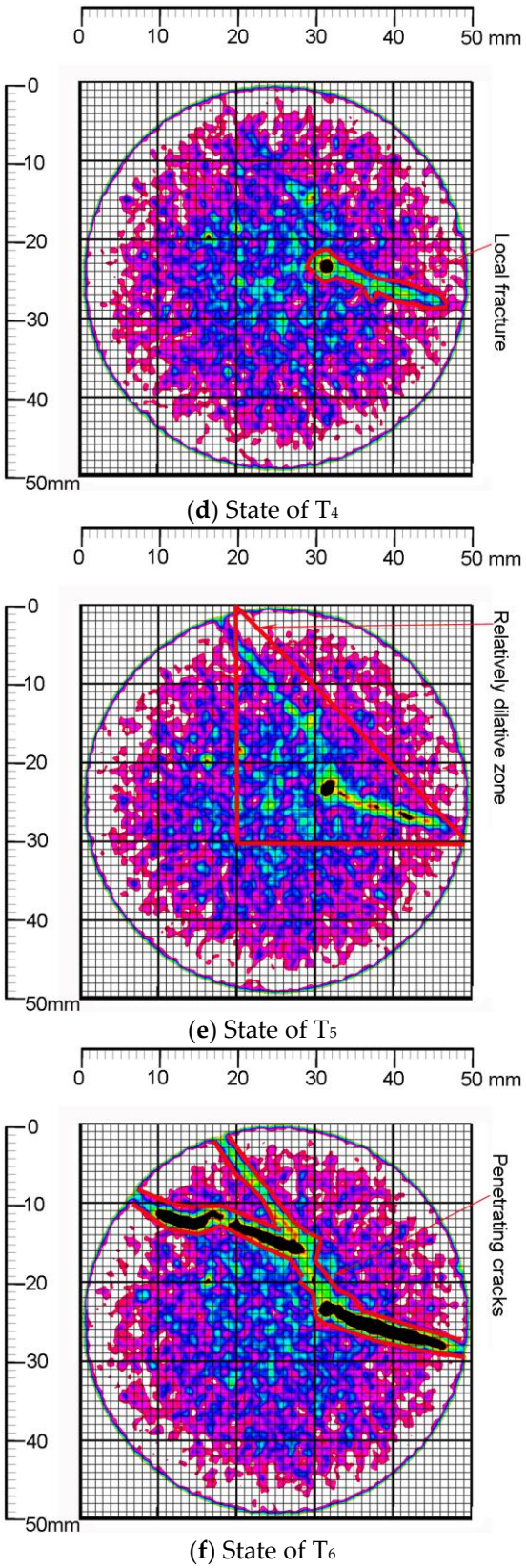

Figure 18. Reconstructed models of damage evolution of the normal cylinder specimen

Particularly, by the help of the marginal points, the characteristics of the marine mortar were introduced according to Figure 17 interval by interval as follows.

Interval 0-A on the curves in Figure 17 The value of ε_a in the direction of the axial load σ_a was 0 at point A where the driving shaft (i.e., the vertical main-shaft) under the parking state had no any motion and the axial load has not been worked. The confining load of 2 MPa (i.e., σ_c =2 MPa), by contrast, has been worked on the normal cylinder specimen at the same time in order to stabilize the

Peer-reviewed version available at Materials 2019, 12, 1799; doi:10.3390/ma12111799

radial stress state which demonstrated the storage environment of the material. The priority of the confining load has been accepted by most tri-axial experiments because it can simulate principally the original storage environments of the goal materials then the undisturbed performance in the host of which could be recovered during the tri-axial experiments. Hence, this procedure was defined as stress maintenance. Consequently, the volumetrically contractive strain at point A was 5.09×10^{-5} which was produced by the radial deformation the value of the radially compressive strain of which was -2.59×10^{-5}. Furthermore, the volumetrically contractive strain of interval 0-A showed the linearity of the marine mortar. Meanwhile, the original state of the normal cylinder specimen ((a) in Figure 18) expressed that the temporary compression of the parental focus in the marine mortar contributed to the linearly volumetric contraction.

Interval A-B on the curves in Figure 17 The value of the radial strain ε_r of interval A-B (including point A) in the direction of the confining load σ_c was the minus one which indicated that the radius of the normal cylinder specimen has been compressed to be the shorter one. The range of the minus strain value was $[-2.17\times10^{-5}, 0)$ where -2.17×10^{-5} was the value of the radially compressive strain of point B on 3rd curve of Figure 17. Meantime, the axial strain here which was produced by the axially compressive deformation accumulated up to 1.96×10^{-3} (at point B on 1st curve of Figure 17) and the maximally volumetric strain of interval A-B attained 1.99×10^{-3} (at point B on 2nd curve of Figure 17). Hence, it can be deduced that the totally volumetric deformation here was the contractive one in both axial direction and radial direction. Furthermore, the development of the axial strain and the volumetric one showed significantly the linear and the non-linear characteristics, respectively. Meanwhile, the radial strain here also developed non-linearly. Consequently, the non-linearity of the volumetric strain has been caused by the non-linearly radial strain the contribution to which was the micro-cavities' compaction in Figure 19. The gel-like constituents around the micro-cavities (including C-S-H and Friedel's salt) were locked in the radial direction, which created the non-linearly radial strain.

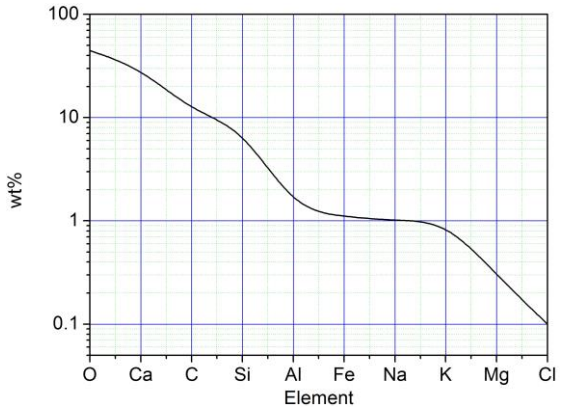

(**a**) EDS spectrum of the micro-cavities

Peer-reviewed version available at Materials 2019, 12, 1799; doi:10.3390/ma12111799

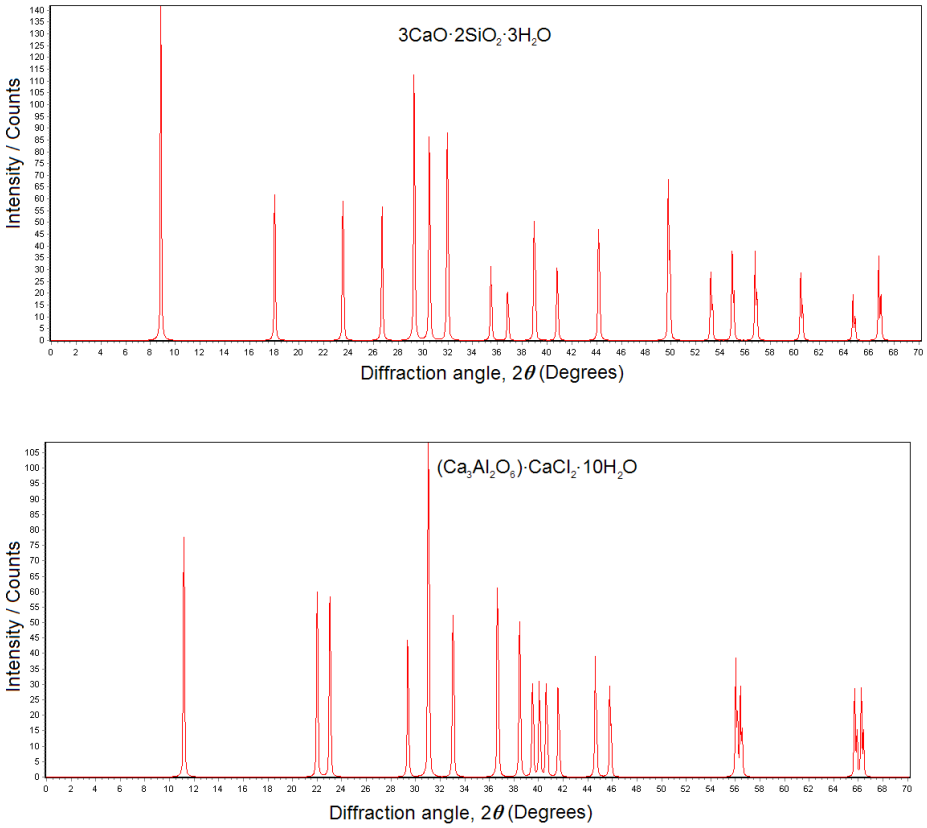

(**b**) XRD patterns of the micro-cavities

(**c**) SEM state at point A

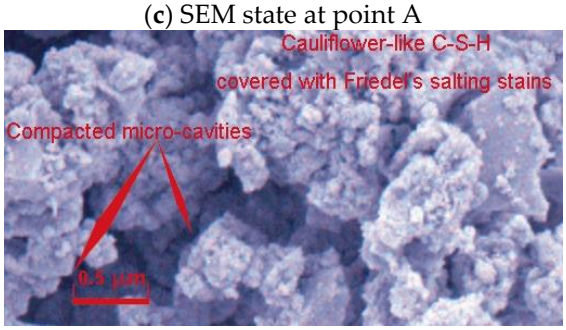

(**d**) SEM state at point B

Figure 19. Behaviors of micro-cavities in the marine mortar

The generation of the hydrate and the salt in Figure 19 was interpreted by the following equations.

$$2\left(Ca_3SiO_5\right)+6H_2O=3CaO\cdot 2SiO_2\cdot 3H_2O+3Ca\left(OH\right)_2 \quad (3)$$

$$Ca\left(OH\right)_2+2NaCl=CaCl_2+2Na^+ +2OH^- \quad (4)$$

$$Ca_3Al_2O_6+CaCl_2+10H_2O\rightarrow\left(Ca_3Al_2O_6\right)\cdot CaCl_2\cdot 10H_2O \quad (5)$$

Peer-reviewed version available at Materials 2019, 12, 1799; doi:10.3390/ma12111799

Interval B-C on the curves in Figure 17 In terms of the direction of σ_1 (i.e., the direction of the axial load σ_a), the peak strength of the marine mortar was 33.88 MPa that was indicated by point C on the three curves in Figure 17. The values of the axial strain ε_a and the volumetric one ε_v here were 1.23 ×10^{-2} and 1.0 ×10^{-2} (indicated by point C on the 1st and 2nd curves in Figure 17), respectively. Correspondingly, they accounted for 62.11% and 95.61% of their peak values (denoted by point D on the 1st and 2nd curves). Meantime, the radial strain at point C in the 3rd curve was 1.09×10^{-3}. Particularly, the axial strain of the interval B-C was produced by the compressive deformation in the direction of σ_1. On the contrary, the radial strain of the interval B-C was produced by the tensile deformation in the direction of σ_c. Moreover, the volumetric strain of the interval B-C has been generated by the global contraction of the normal cylinder specimen. Therefore, the conclusions deduced from the characteristics of the interval B-C included that the development of the peak strength would consume more than half of the axially compressive strain and most of the volumetrically contractive strain of the marine mortar; however, the radial strain with the softly loading condition (by the oil pressure) was under-developed when the marine mortar reached its peak strength of the σ_1 direction; the radial strain here, at the same time, indicated the absolutely tensile deformation in the σ_c direction; hence, the axial compression has dwarfed the radial extension and generated resultantly the global contraction of the normal cylinder specimen. Meanwhile, the MSHCT state of the normal cylinder specimen ((b) in Figure 18) showed that the distribution of the cohesive continuum around the parental focus has been disturbed explicitly and the promising damage zones have been fused to be a connectively larger area in the core of which the outline of the parental focus was squeezed to be a smooth configuration. Moreover, a new baby focus was generated at the 12 o'clock direction of the parental one at the position T_3 where the distance between the parental focus and the new baby was 11.31mm and the connective area was destroyed to be the fragments ((c) in Figure 18).

Interval C-D on the curves in Figure 17 The axial strain ε_a and the volumetric one ε_v reached their peak values (indicated by point D on the 1st and 2nd curves) at the same stress state where σ_1 =20.34 MPa at the backbone of the hysteresis loop in Figure 17. The peak values of ε_a and ε_v were 1.61×10^{-2} and 1.14×10^{-2}, respectively. Meantime, the strength of the marine mortar began to drop after the peak strength (represented by point C on the three curves in Figure 17) steeply towards the strain coordinate axis. On the other side, the axially compressive strain of interval C-D still increased along the negative direction of the σ_1 coordinate axis. Similarly, the radial strain here that was caused by the tensile deformation showed the reversely climbing trend when compared with the radial strain of interval B-C. In contrast, there lived at position T_5 of 2nd curve a locally odd fall which indicated the relatively dilative deformation. Furthermore, the locally high-angle zones happened at the very position 6 of both the axial strain curve and the radial strain one (namely, the 1st and 3rd curves in Figure 17). Especially, the locally odd fall on the 2nd curve triggered the fluctuation of the volumetric strain around it which denoted the alternate deformations of the volumetric contraction and dilation. Therefore, it can be confirmed that the local fractures that thus presented the abruptly volumetric deformation have burst in the normal cylinder specimen ((d) in Figure 18); the locally steep rise of the radially tensile strain defeated that of the axially compressive strain, which created the relatively dilative deformation of the marine mortar (at position T_5 of 2nd curve and (e) in Figure 18). The local fracture in Figure 18 that caused the abruptly volumetric dilation was built by three zones, namely, the interface failure zone where the marine sand particle was pulled half out of the hydrate layers and the framework of the marine mortar was collapsed, the crack zone where the hydrate layers including mainly C-S-H, C-A-S-H and N-A-S-H gel were broken partially into a volumetric crack, and the breakage zone where the needle-like AFt (namely, ettringite) was snapped and its clastic ones clogged and enlarged the volumetric crack with the coupled effects of its growth and the load (Figure 20).

Peer-reviewed version available at Materials 2019, 12, 1799; doi:10.3390/ma12111799

(**a**) Local fracture

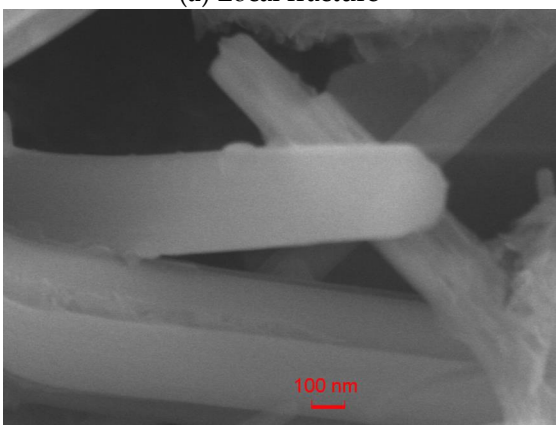

(**b**) Detail of AFt

Figure 20. SEM image of the local fracture and volumetric dilation

Especially, the perimeter of the marine sand particle that was pulled half out of the hydrate layers was covered with the salt chips which precipitated the interfacial damage in the crack zone due to the shortage of smaller marine sand particles that could help absorb the salt chips.

Interval D-E on the curves in Figure 17 The axial strain ε_a began to drop after the peak value 1.61×10^{-2} and the principal stress σ_1 at point E of the three curves in Figure 17 was 13.53 MPa with the correspondingly axial strain 1.5×10^{-2} where the framework of the normal cylinder specimen began to crumble due to the re-adjustment of ε_a development. The re-adjustment of ε_a development produced the loose connection among the macro-fragments and undermined the marine mortar's strength. Meanwhile, the smart extensometer of the tri-axial sub-system decelerated tracing the axial deformation to prohibit the injury against the sub-system and then the driving shaft started to rest here gradually. Hence, the dropping trend of the axially compressive strain coupled with the strength reduction represented that the axially tensile deformation was recovered marginally as a result of the gradual rest of the vertical main-shaft which helped retrieve partially the elasticity of the marine mortar. Moreover, σ_c here failed to confine effectively the radially tensile deformation due to the crumbled framework of the normal cylinder specimen. The maximal gradient of the radial tensile strain with the axial load (i.e., ε_r / σ_a) resided at interval D-E and the value was 4.03×10^{-4}/MPa that indicated the relatively volumetric dilation of the marine mortar. The 2nd curve in Figure 17 showed that maximal value of the relatively volumetric dilative strain at interval D-E was 4.94×10^{-3} which denoted that the confining load σ_c could not resist the volumetric dilation in radial direction again. Particularly, the partially retrieved elasticity in the axial direction also contributed to the relatively volumetric dilation of the marine mortar the framework of which has been radically re-organized during the elastic recovery.

Interval E-F on the curves in Figure 17 The strength of the normal cylinder specimen was softened by the penetrating cracks ((f) in Figure 18) at interval E-F. Meantime, the framework of the

Peer-reviewed version available at Materials 2019, 12, 1799; doi:10.3390/ma12111799

normal cylinder specimen absolutely collapsed due to the widespread microscopic deterioration (namely, the foci in Figure 21).

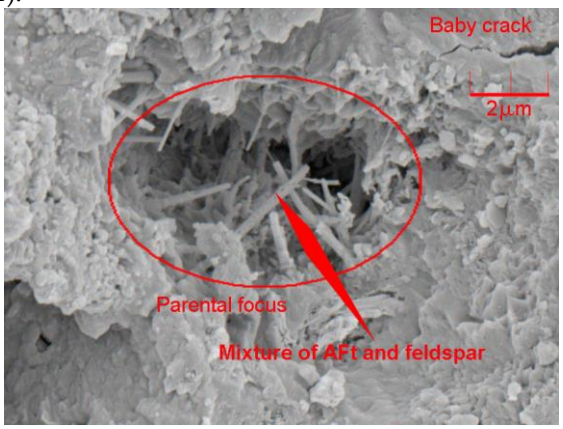

(**a**) Parental focus with its baby crack in 2 o'clock direction

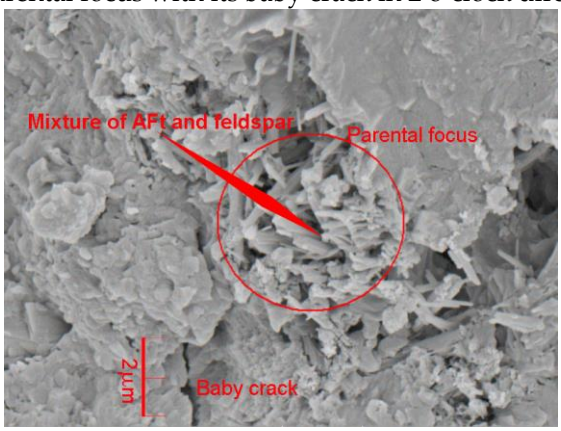

(**b**) Parental focus with its baby crack in 6 o'clock direction

Figure 21. SEM images of microscopic deterioration due to the foci development

The generation of Aft and feldspar mixture formed the well-blockage in the marine mortar where the hydration was retarded locally and the discontinuous foci were created under the loading conditions. The discontinuous foci at the initially loading stage were supported by the stick-like elements of Aft and feldspar mixture. Eventually, the elements were crashed radically into chips and the local hydrate that was the constraint boundary of the foci at the initially loading stage was collapsed due to the fatigue damage which caused the evolution of the baby cracks. Therefore, the foci neighborhood deteriorated thoroughly with loss of the bracement from the local hydrate and Aft and feldspar mixture. The procedure on the widespread microscopic deterioration in the marine mortar can be depicted by Figure 22 as follows.

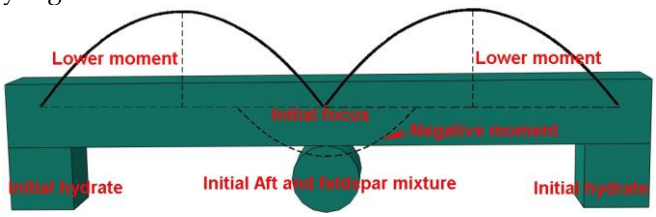

(**1**) Initial state when the local hydrate and Aft and feldspar mixture offered reliably the constraint

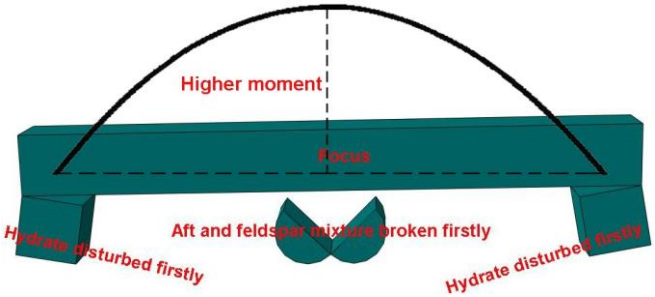

Peer-reviewed version available at Materials 2019, 12, 1799; doi:10.3390/ma12111799

(**2**) First breach against the local hydrate and Aft and feldspar mixture

(**3**) First damage of the focus

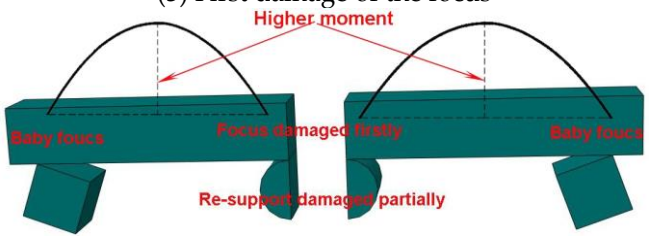

(**4**) Re-support from the local hydrate and Aft and feldspar mixture which has been damaged partially

…

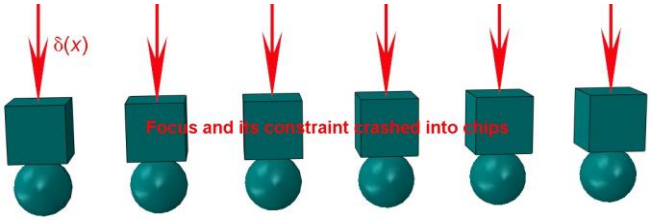

(**n**) Absolute loss of the bracement from the local hydrate and Aft and feldspar mixture

Figure 22. Widespread microscopic deterioration model

The focus and its constraint from the local hydrate and Aft and feldspar mixture formed the hyper-static framework under the initial state where the moments in the focus were the lower ones and the microscopic deterioration in the marine mortar did not spread yet ((1) in Figure 22). Meantime, the moments here could be defined by the parabolic functions with the postulation that the uniform load worked on the focus the volume of which was the infinitesimal one. However, the focus failed to be solidified with its constraint as the result of the discontinuousness which blocked the locally advanced hydration. The cumulative load broke the stick-like elements of Aft and feldspar mixture isolated from the hydration, by which, the framework formed by the focus and its constraint became the statically determinate one with the higher moment ((2) in Figure 22). The focus thereby was damaged to be the baby ones that were loaded with the higher moment and the local hydrate that was the constraint boundary of the baby foci was also disturbed ((3) and (4) in Figure 22). Moreover, the baby foci with their constraint always formed the unreliable framework of the statically determinate one from then on and the breach of the framework kept going due to the higher moments until the stick-like elements were crashed radically into chips. The foci then had to stand on the chips and sustained the infinitely concentrated load which could be expressed by Dirac function in Equation (6). Consequently, the microscopic deterioration spread out of control ((n) in Figure 22).

$$\delta(x)=\begin{cases}\dfrac{1}{2\xi} & |x|\le\xi\\ 0 & |x|>\xi\end{cases} \tag{6}$$

where x denoted the possibly loading domain; ξ represented the foci neighborhood that approached the infinitesimal. Hence, the nano-scale foci can deteriorate easily due to the infinite load of $\delta(x)$.

Particularly, the resilient performance of the axial load at interval E-F did not mean that the strength of the marine mortar was retrieved. Coupled with the unconfined extension in the radial direction (3rd curve in Figure 17), the re-increment of the axial strain (1st curve in Figure 17) indicated the volumetric dilation of the marine mortar out of control, with which, the resilient performance of

Peer-reviewed version available at Materials 2019, 12, 1799; doi:10.3390/ma12111799

the axial load caused the absolute collapse of the framework of the normal cylinder specimen instead of the strength retrieve. The residually axial load σ_a at position F was 13.64 MPa. Correspondingly, the axial strain ε_a, the volumetric strain ε_v and the radial one ε_r here were 1.52×10^{-2}, 5.19×10^{-3} and 4.95×10^{-3}, respectively.

4. Conclusions

In this study, the on-line multi-scale damage detection experiments accompanied with EDS, XRD and SEM analysis were implemented to evaluate the multi-scale physical-chemical-mechanical characteristics of the marine mortar. The following conclusions based on them can be drawn:

1. The main source of the saline minerals in the marine mortar was the seawater used for the specimens' preparation. The saline minerals in the marine mortar were dissipated partly as a result of the curing treatment. However, the residual saline minerals generated the micro-interfacial flaws coupled with the uniform and discontinuous distribution of the marine sand.
2. The local fracture in the marine mortar could be controlled by the active adjustment for the distribution of the marine sand. The bigger marine sand particles could strengthen the framework of the marine mortar and the smaller ones played the key role in residual saline minerals' absorption.
3. The micro-interfacial behavior of the marine sand and the hydrate gel controlled partially the performance of the marine mortar. The factors inclusive of the curing, the surface of the marine sand and the gel type worked crucially on the micro-interfacial behavior, which should be studied specifically.
4. The principal constituents of the composite Portland cement P.C 42.5 R included Ca_2SiO_4, Ca_3SiO_5 and $Ca_3Al_2O_6$ that contributed to the hydrate generation of the marine mortar.
5. The cause why the on-line multi-scale damage detection experiments art was designed is that the art helps quantify the multi-scale damage evolution of the marine mortar mathematically and graphically.
6. According to the results from the on-line multi-scale damage detection experiments, the priority of the confining load produced the linearly volumetric contraction due to the temporary compaction of the parental foci in the marine mortar. Particularly, the radially compressive deformation was the only contribution to the linearly volumetric contraction during the stress maintenance.
7. With the birth of the axial strain, the gel-like constituents around the micro-cavities began to be softened, which created the non-linearly radial strain. Meanwhile, the non-linearly radial strain triggered the development of the non-linearly volumetric deformation of the marine mortar.
8. The normal cylinder specimen was scanned for 2 times besides the original state scan before the peak strength of the marine mortar which was 33.88 MPa. The development of ε_a and ε_v here accounted for more than half of their peak values, by which, the kneaded parental focus gave birth to a baby one. Consequently, the connective marine mortar between them was destroyed to be the fragments by the resultantly global contraction.
9. ε_a and ε_v achieved their peak values at the same stress state where their values were 1.61×10^{-2} and 1.14×10^{-2}, respectively. There lived between the peaks of ε_a (or ε_v) and σ_1 the locally high-angle zones of the SSS curves and the local fractures were produced right here. Particularly, the abruptly volumetric dilation was caused by the local fractures composed of the interface failure zone of SiO_2, the crack zone of the hydrate layers and the breakage zone of the needle-like Aft. Moreover, the radial tensile strain met a sharp knee corner right in the position where ε_a and ε_v achieved their peak values. The ε_r development dashed out of control afterwards. Coupled with the maximal gradient of the radial tensile strain with the axial load, the partially retrieved elasticity in the axial direction caused the relatively volumetric dilation of the marine mortar.
10. Upon the penetrating cracks' birth, deteriorated thoroughly was the neighborhood of the parental foci where the widespread microscopic failure destroyed the reliable support from the

Peer-reviewed version available at *Materials* **2019**, *12*, 1799; doi:10.3390/ma12111799

local hydrate and the mixture of Aft and feldspar. Consequently, the parental foci with the discontinuousness and the well-blockage effect triggered the Domino damage in the marine mortar.

11. The development of ε_a, ε_v and ε_r achieved the coupled effect in the marine mortar performance although their behaviors showed the different characteristics. The synchronization of SSS metrization and damage visualization established in this study was the crucial approach for the research on the multi-scale physical-chemical-mechanical characteristics of the marine mortar.

Author Contributions: Conceptualization, Yajun WANG; methodology, Yajun WANG and Youbo WANG; software, Yajun WANG and Qian YAN; validation, Chuhan ZHANG; formal analysis, Chuhan ZHANG and Jinting WANG; investigation, Yajun WANG, Xiaoqing GAN and Youbo WANG; resources, Yajun WANG, Youbo WANG and Qian YAN; data curation, Youbo WANG, Qian YAN and Tao LIU; writing-original draft preparation, Yajun WANG; writing-review and editing, Jinting WANG and Feng JIN; visualization, Yajun WANG, Qian YAN and Zhan XIONG; supervision, Chuhan ZHANG; project administration, Yajun WANG and Yanjie XU; funding acquisition, Yajun WANG and Yanjie XU.

Funding: This research was funded by National Natural Science Foundations of China, grant numbers 51879236 and 51109118 and Open Research Fund Program of State key Laboratory of Hydroscience and Engineering, grant number sklhse-2018-E-03.

Conflicts of Interest: The authors declare no conflict of interest.

References

1. https://www.worldcement.com/ (accessed on 03.05.2019)
2. https://www.gain.ie/ (accessed on 03.05.2019)
3. https://www.sand.org/ (accessed on 03.05.2019)
4. https://www.wri.org/ (accessed on 03.05.2019)
5. Li, Y.L.; Zhao, X.L.; Singh, R.K.R.; Al-Saadi, S. Experimental study on seawater and sea sand concrete filled GFRP and stainless steel tubular stub columns. *Thin. Wall. Struct*. 2016, 106, 390-406.
6. Wang, Z.K.; Zhao, X.L.; Xian, G.J.; Wu, G.; Singh, R.K.R.; Al-Saadi, S. Effect of sustained load and seawater and sea sand concrete environment on durability of basalt- and glass-fibre reinforced polymer (B/GFRP) bars. *Corros. Sci*. 2018, 138, 100-218.
7. Yang, S.T.; Xu, J.J.; Zang, C.H.; Li, R.; Yang, Q.B.; Sun, S.G. Mechanical properties of alkali-activated slag concrete mixed by seawater and sea sand. *Constr. Build. Mater*. 2019, 196, 395-410.
8. Zhou, A.; Qin, R.Y.; Chow, C.L.; Lau, D. Structure performance of FRP confined seawater concrete columns under chloride environment. *Compos. Struct*. 2019, 216, 12-19.
9. Yang, J.M.; Tang, Q.Q.; Wu, Q.S.; Li, X.H.; Sun, Z.X. The effect of seawater curing on properties of magnesium potassium phosphate cement. *Constr. Build. Mater*. 2017, 141, 470-478.
10. Yang, J.M.; Zhang, J.; Zheng, S.C. Experimental research on seawater erosion resistance of magnesium potassium phosphate cement pastes. *Constr. Build. Mater*. 2018, 183, 534-543.
11. Fraternali, F.; Spadea, S.; Berardi, V.P. Effects of recycled PET fibres on the mechanical properties and seawater curing of Portland cement-based concretes. *Constr. Build. Mater*. 2014, 61, 293-302.
12. Wang, J.J.; Liu, E.G.; Li, L. Multiscale investigations on hydration mechanisms in seawater OPC paste. *Constr. Build. Mater*. 2018, 191, 891-903.
13. Shi, Z.G.; Geiker, M.R.; Lothenbach, B.; Weerdt, K.D.; Garzón, S.F.; Enemark-Rasmussen, K.; Skibsted, J. Friedel's salt profiles from thermogravimetric analysis and thermodynamic modelling of Portland cement-based mortars exposed to sodium chloride solution. *Cement. Concrete. Comp*. 2017, 78, 73-83.
14. Yu, C.J.; Wu, Q.; Yang, J.M. Effect of seawater for mixing on properties of potassium magnesium phosphate cement paste. *Constr. Build. Mater*. 2017, 155, 217-227.
15. Yang, J.M.; Zhang, J.; Zheng, S.C. Experimental research on seawater erosion resistance of magnesium potassium phosphate cement pastes. *Constr. Build. Mater*. 2018, 183, 534-243.
16. Yang, J.M.; Tang, Q.Q.; Wu, Q.S.; Li, X.H.; Sun, Z.X. The effect of seawater curing on properties of magnesium potassium phosphate cement. *Constr. Build. Mater*. 2017, 141, 470-478.
17. Li, Y.L.; Zhao, X.L.; Singh, R.K.R.; Al-Saadi, S. Thermal and mechanical properties of alkali-activated slag paste, mortar and concrete utilising seawater and sea sand. *Constr. Build. Mater*. 2018, 159, 704-724.

Peer-reviewed version available at *Materials* **2019**, *12*, 1799; doi:10.3390/ma12111799

18. Wang, Y.Y.; Shui, Z.H.; Gao, X.; Huang, Y.; Yu, R.; Li, X.S. Utilizing coral waste and metakaolin to produce eco-friendly marine mortar: Hydration, mechanical properties and durability. *J. Clean. Prod*. 2019, 219, 763-774.
19. Tan, Y.S.; Yu, H.F.; Mi, R.J.; Zhang,Y. Compressive strength evaluation of coral aggregate seawater concrete (CAC) by non-destructive techniques. *Eng. Struct.* 2018, 176, 293-302.
20. Guo, F.; Al-Saadi, S.; Singh, R.K.R.; Zhao, X.L. Durability of fiber reinforced polymer (FRP) in simulated seawater sea sand concrete (SWSSC) environment. *Corros. Sci*. 2018, 141, 1-13.
21. Ministry of Construction of the PR China, Standard for technical requirements and test method of sand and crushed stone (or gravel) for ordinary concrete JGJ 52-2006, Beijing, 2006 [in Chinese]
22. ASTM D1141-98. Standard Practice for the Preparation of Substitute Ocean Water; ASTM International: West Conshohocken, PA, US, 2013.
23. ASTM C1084-10. Standard test method for Portland-cement content of hardened hydraulic-cement concrete; ASTM International: West Conshohocken, PA, US, 2010.
24. ASTM C1180-18. Standard Terminology of Mortar and Grout for Unit Masonry; ASTM International: West Conshohocken, PA, US, 2018.
25. ASTM C270-19. Standard Specification for Mortar for Unit Masonry; ASTM International: West Conshohocken, PA, US, 2019.
26. ASTM C305-14. Standard Practice for Mechanical Mixing of Hydraulic Cement Pastes and Mortar of Plastic Consistency; ASTM International: West Conshohocken, PA, US, 2014.